



Flexible arc-shaped triboelectric nanogenerator for all directions and highly efficient biomechanical energy harvesting and human motion monitoring

Dali Yan ^{a,1}, Dan Tao ^{a,1}, Duo Xu ^{a,1}, Yirong Sun ^a, Bo Deng ^{a,*}, Genyang Cao ^{a,*}, Jian Fang ^b, Weilin Xu ^a

^a State Key Laboratory of New Textile Materials and Advanced Processing Technologies, Wuhan Textile University, Wuhan, Hubei 430200, PR China

^b College of Textile and Clothing Engineering, Soochow University, Suzhou 215123, PR China



ARTICLE INFO

Keywords:

Triboelectric nanogenerator
Angular dependence
All directions harvester
Three-dimensional textiles

ABSTRACT

As an environmentally friendly and renewable energy source, triboelectric nanogenerator (TENG) offers a fresh solution to the energy scarcity problem. However, the conventional three-dimensional (3D) TENG, which exhibits heavy angular dependence in energy harvesting, struggles to efficiently capture complex biological kinetic energy in practical applications. This study addresses this challenge by developing a novel flexible arc-shaped triboelectric nanogenerator (F-TENG). In comparison with traditional 3D flexible-based TENG, this generator notably minimizes the angular dependence on motion direction. Particularly for non-vertical mechanical energy harvesting, F-TENG can enhance collection efficiency by 35.5 %. Experimental results demonstrate that the open-circuit voltage and current of F-TENG textiles are 3 times and 2.6 times higher, respectively than those of conventional 3D flexible-based TENG. Its accuracy in detecting and identifying complex motions reaches 86.8 %, marking a 37.8 % improvement over traditional 3D-TENG. This study presents a promising perspective on the structural design of all directions and highly efficient biomechanical energy harvesting and its application in the field of intelligent sensing.

1. Introduction

The triboelectric nanogenerator (TENG), as an eco-friendly and renewable green energy source, exhibits immense potential in the fields of energy harvesting and wearable energy [1,2]. Among various types of TENG devices, textiles have emerged as ideal substrates due to their ideal conformity to the human body [3,4]. Since the invention of metal-free fiber-based TENG by Zhong [5], the structure, performance, and applications of flexible-based TENG have been extensively investigated [6]. Some researchers claim that the vertical contact-separation mode is the most effective mode for harvesting mechanical energy extensively from the human body [7]. For instance, mechanical energy generated from activities like walking or running can be converted into electrical energy through TENG embedded in shoe soles or insoles. Furthermore, the output of TENG largely depends on the displacement deformation of triboelectric materials under different compression stresses [8,9]. Traditional three-dimensional (3D) TENG, primarily based on the contact-separation mode, requires a gap to accommodate

this deformation, thus converting the periodic triggering of TENG into periodic contact-separation between triboelectric layers [10]. However, traditional 3D-TENG generally adopts a "sandwich" structure [11,12], which inherently exhibits angular dependence in the collection of motion energy [13] (Fig. 1a1). That is, when subjected to compressive stress from different directions, only the vertical pressure can effectively act on the gap, thereby enabling periodic contact separation between triboelectric layers, resulting in alternating current. When subjected to non-vertical compressive stress, only the vertical component of the motion could be collected [14]. The horizontal component of the force, due to boundary constraints, cannot generate horizontal displacement, thus being unable to harvest biological motion energy in that direction (Fig. 1a2), leading to the low energy collection efficiency of traditional 3D-TENG.

Some researchers have tried to enhance energy collection efficiency by studying the compressive deformation of traditional 3D textile structures. For instance, Li et al. [9] investigated the impact of different connection angles of spacer yarns on output performance under stress

* Corresponding authors.

E-mail addresses: dengjianguo88@outlook.com (B. Deng), genyang.cao@wtu.edu.cn (G. Cao), jian.fang@suda.edu.cn (J. Fang).

¹ These authors contributed equally to this work.

and developed "sandwich" flexible-based TENGs with different spacer structures. Ding et al. [15] proposed a hollow spherical arch structure based on alveolar deformation characteristics, which converts vertical pressure into horizontal thrust, thereby increasing effective contact area and improving output performance. However, their work only investigated energy collection in the vertical direction. Many researchers have recognized that a critical reason for the low energy collection efficiency is the severe angular dependence of traditional 3D textiles in energy collection, meaning that traditional 3D textiles can only deform under force in a specific direction, thus only collecting unidirectional motion energy [16]. To overcome the angular dependence in collecting motion energy, Liang et al. devised a spring-assisted system based on a spherical TENG for capturing wave energy, enabling energy collection from multiple directions and enhancing the collection of random and irregular wave energy [17]. Paosangthong et al. proposed an all-directions flexible-based TENG that collects energy from sliding in any direction inside the plane. This structure overcomes the directional dependence of traditional grating/weaving structures, which can only collect energy from a single direction [18]. While their proposed all-direction energy harvesting is still limited to energy generated in-plane sliding mode. In the current state of TENG research [19–21], most of the work ignored the angular dependence of energy harvesting by 3D-TENGs, especially in the contact separation mode.

Most flexible-based TENG currently use rigid metal electrodes such as gold [22,23], copper [24,25], stainless steel [26], or metal thin film electrodes [27], which suffer from the following significant drawbacks. Firstly, they are prone to fatigue failure after repeated deformations, leading to poor durability [28]. Secondly, the poor adhesion between metals or metal thin films and textiles affects the stability and durability of TENG device [29]. To overcome this limitation, core-shell structured yarns, utilizing commercial silver-plated nanowires as core and polyimide (PI)/wool as shell, were braided together on a high-speed braiding machine. Core-shell yarns offer the following advantages: the yarn structure exhibits higher flexibility as textile, enabling better adaptation to complex environments and deformation states [30]. Furthermore, the design of the core-shell structure provides effective protection for the conductive yarn, enhancing fatigue resistance and extending the

lifespan of the TENG [31].

In this study, a novel 3D arc structure textile was designed by weaving core-shell yarns, which significantly reduces the angular dependence in energy collection, resulting in a 35.5 % improvement in energy harvesting efficiency relative to the traditional sandwich-type TENG, and achieving a multi-angle harvest of biological motion energy and self-powered sensing (Fig. 1b1). Simultaneously, this arc structure utilizes air as the gap, thereby avoiding the influence of spacer materials on output performance [9,10] (Fig. 1b2). To discuss the influence of arc structure parameters, we introduce the concept of projection ratio, defining the ratio of the projected area of the arc structure layer (πN^2) to the effective contact area of the bottom layer (πL^2) as the projection ratio P (Fig. 1c). By adjusting the projection ratio P, the contact-separation distance between triboelectric layers and the effective contact area can be effectively controlled simultaneously, optimizing the output of TENG. Additionally, we apply the arc-shaped TENG (F-TENG) to a plantar pressure sensing system, utilizing the YOLOv5 algorithm to learn and train the signals collected from the insoles, thereby achieving recognition of human gait and motion health detection. Due to its outstanding performance in collecting energy from different motion directions, it enhances the signal-to-noise ratio and consequently achieves a higher recognition accuracy for complex human motion (86.8 %, a 37.8 % improvement compared to conventional sandwich-type TENGs).

2. The operating principle of the 3D F-TENG

The operating mechanism of F-TENG is based on the coupling effect of contact electrification and electrostatic induction. F-TENG employs silver-coated nanowires as electrodes, with wool and polyimide as triboelectric layers, operating in a vertical contact-separation mode. The power generation mechanism of F-TENG is illustrated in Fig. 2a. In the initial state, the two triboelectric layers are not in contact, no charge is generated, and there is no potential difference between the two electrodes (State I). When wool and polyimide come into contact under an external force, equal amounts of positive and negative triboelectric charges are generated on the surfaces of the two triboelectric layers

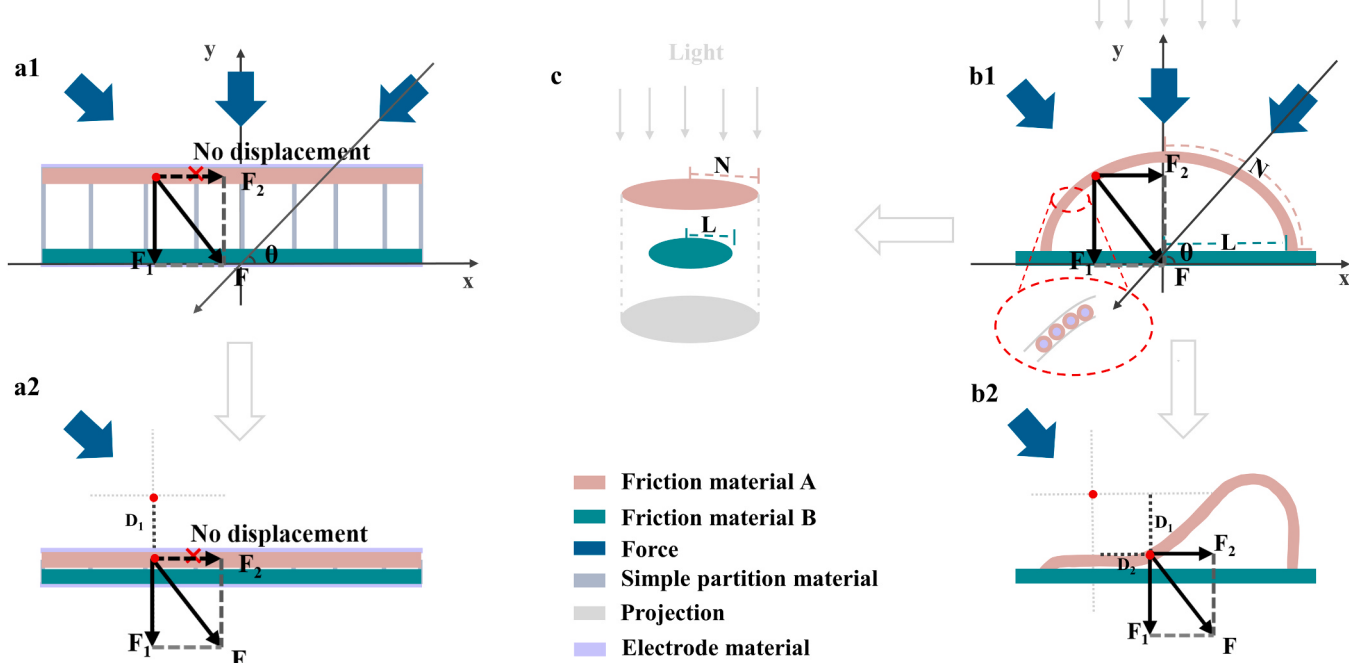


Fig. 1. Illustrative comparison between traditional 3D flexible-based TENG and 3D F-TENG. (a1-a2) Analysis of stress and displacement in traditional 3D flexible-based TENG; (b1-b2) Analysis of stress and displacement in 3D F-TENG; (c) Schematic projection ratio of 3D arc-shaped fabric.

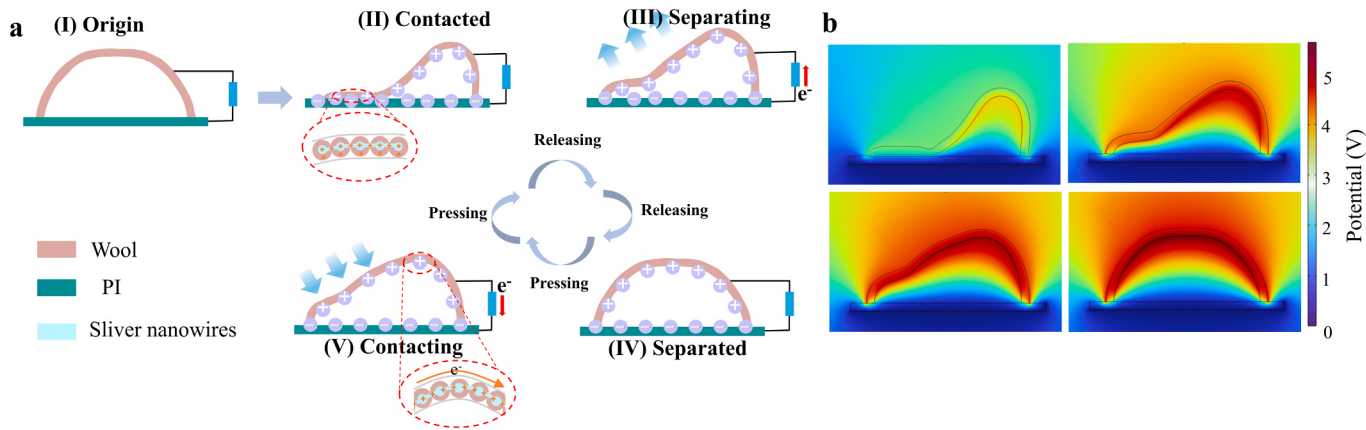


Fig. 2. Depicts the operational principle of 3D F-TENG. (a) Schematic diagram illustrating the operational principle; (b) COMSOL simulation schematic.

[32]. Since the charges on the surfaces of the two triboelectric layers are in the same plane, there is no potential difference between the two electrodes, and electrons do not flow in the external circuit (State II). Once the external force disappears, the separation of the two surfaces creates a dipole moment, forming a potential difference that drives electrons through the external circuit from the electrode of the electronegative material to the electrode of the electropositive material (State III). Finally, when the two triboelectric layers are completely separated, a dynamic equilibrium is reached (State IV). When the two triboelectric layers are subjected to external force again, the electrostatic induction charges flow back through the external circuit (State V) until the two triboelectric layers are in full contact again [33,34]. To further verify the working mechanism of F-TENG, we conducted finite element simulations to more intuitively display the electrostatic potential distribution of the sample in different states, as shown in Fig. 2b.

In contact-separation TENGs, both the relative motion distance and effective contact area of the triboelectric layers affect the electrical performance. According to the following formulas (1) and (2), it is evident that when the bottom width ($2L$) of the arc structure is fixed, a longer arc length (N) and smaller radius (R) result in a greater contact distance (H) (Fig. S1). Therefore, we can regulate the output performance of the TENG by adjusting L , N , R , and H of the arc structure.

$$\sin\left(\frac{N}{R}\right) = \frac{L}{R} \quad (1)$$

$$R^2 = L^2 + (R - H)^2 \quad (2)$$

Analyses of the traditional sandwich model and the 3D arc model are given as follows: As shown in Fig. 1, establish a coordinate axis with the center position of the frictional bottom layer as the origin. The angle between the direction of force and the x-axis is θ . In the interval $(0, \pi)$: when the angle θ is $\pi/2$, the applied force F acts entirely perpendicular between the two layers of triboelectric materials, thus $F_1=F\times\sin(\pi/2)=F$. Here the vertical force causes vertical displacement $D=D_1$. When θ is not equal to $\pi/2$, the force is resolved into vertical component F_1 and horizontal component F_2 according to the parallelogram law. These two components cause the triboelectric layers to undergo vertical displacement D_1 and horizontal displacement D_2 simultaneously. Since traditional 3D flexible-based TENG is constrained by boundaries in the horizontal direction, the horizontal component F_2 cannot generate horizontal displacement D_2 and thus does not contribute to the electrical output of TENG (Fig. 1a2). However, in the flexible arc structure, the horizontal component F_2 can still induce fabric displacement D_2 in the horizontal direction. Through electrostatic induction, this displacement can drive more static charges to flow, thereby enhancing energy collection efficiency (Fig. 1b2). Consequently, the arc structure concurrently collects energy in both horizontal and vertical directions,

significantly reducing its angle dependence on energy collection and thereby achieving higher energy collection efficiency and machine recognition accuracy.

3. Result and discussion

3.1. The structural design and performance analysis of core-shell yarns and 3D F-TENG

To achieve complete wrapping of the conductive yarn, we conducted the calculation based on the diameters of the conductive yarn and the wrapping yarn according to formulas (3) and (4). It can be concluded that a single conductive core yarn can be fully wrapped by eight wrapping yarns, eliminating concerns on the exposure of the conductive yarn leading to charge leakage, as well as excessive wrapping yarns preventing the outer wrapping yarns from contacting the central conductive yarn and thus causing difficulties in charge transfer.

$$\frac{R+r}{\alpha} = \frac{2R}{180^\circ - 2\alpha} \quad (3)$$

$$n = \frac{360^\circ}{\alpha} \quad (4)$$

Here, R represents the radius of the wrapping yarn, r means the radius of the conductive yarn, α refers to the angle formed between the conductive yarn and the wrapping yarn, and n represents the number of wrapping yarns required to wrap the conductive yarn (Fig. S2).

When two different materials come into contact, oppositely charged electric charges accumulate on their surfaces. Since fabrics made of pure wool and polyimide yarn are non-conductive, the charges can only remain on the fabric surface. However, when wool/polyimide yarn is combined with conductive yarn to form core-shell yarn, the conductive yarn in the middle can transfer surface charges, thereby generating electrical output (Fig. 3a). Fig. 3b displays the surface morphology of the core-shell yarn under a 3D microscope and the cross-sectional morphology under an electron microscope when the number of the wrapping yarns increases from 4 to 12. When the conductive yarn is exposed to the air, that is, when there are 4 (Fig. 3b1) or 6 (Fig. 3b2) strands of the outer wrapping yarn, a high humidity environment will cause moisture in the air to carry away a small amount of charge, reducing the electrical output [35]. When there are 8 wrapping yarns, the surface of the core-shell yarn is uniform, and the conductive yarn is completely wrapped by the wrapping yarns (Fig. 3b3). When there are 10 (Fig. 3b4) or 12 (Fig. 3b5) strands of the wrapping yarn, the charges accumulated on the surface of the wrapping yarn have difficulty contacting the conductive yarn in the middle, thus hindering the transfer of charges in the conductive yarn, which also leads to a decrease in electrical output [36].

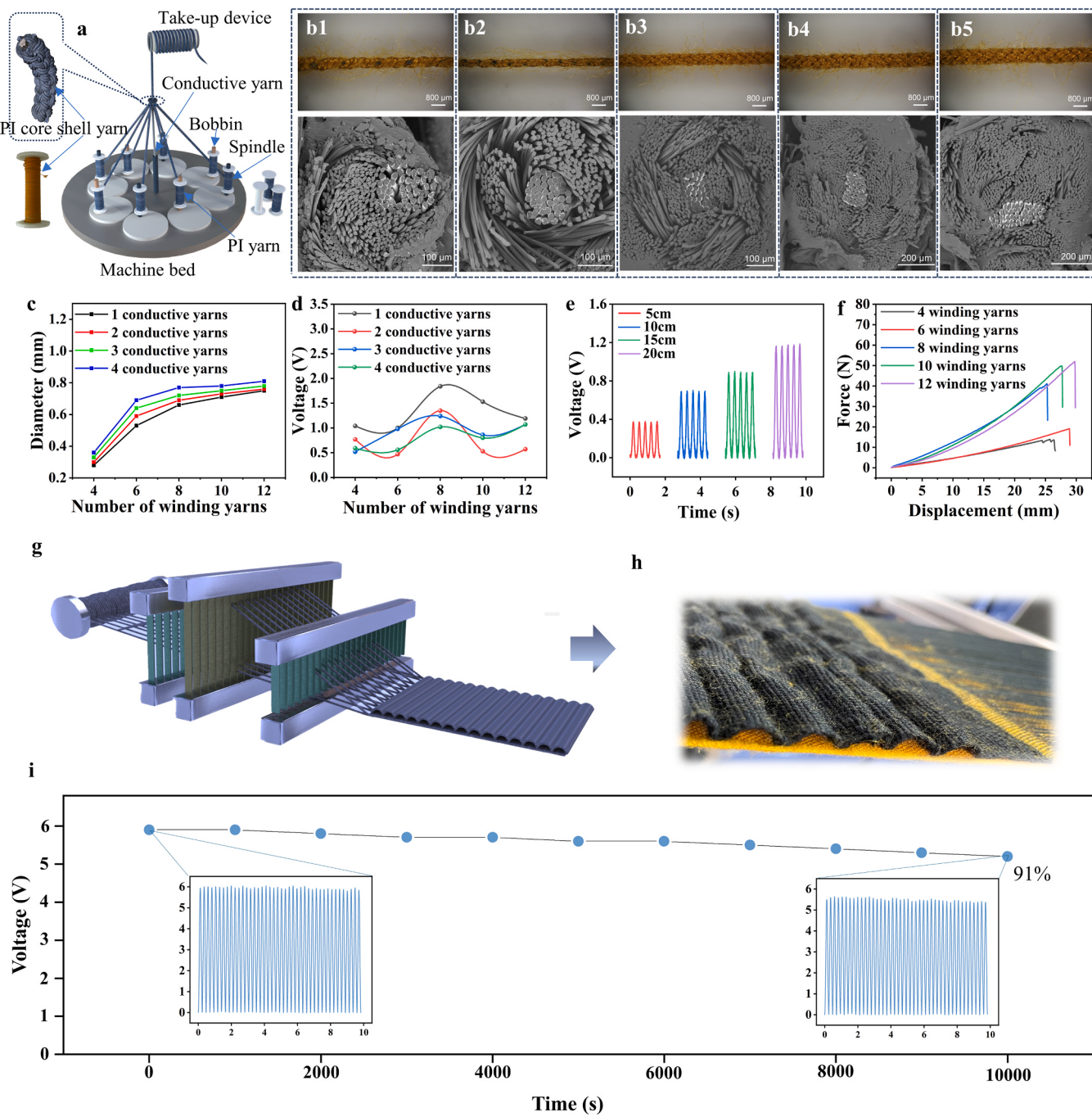


Fig. 3. Presents the structural design and performance analysis of the 3D F-TENG. (a) Schematic diagram of the braiding process of the core-shell yarn. (b) Surface morphology and cross-sectional morphology of the core-shell yarn when the number of wrapping yarns is 4, 6, 8, 10, and 12. (c) The diameter of core-shell yarns is composed of different numbers of conductive yarns and wrapping yarns. (d) The open-circuit voltage of core-shell yarns is composed of different numbers of conductive yarns and wrapping yarns. (e) The open-circuit voltage of core-shell yarns is composed of a single conductive yarn and eight wrapping yarns at different lengths. (f) Force-displacement curves of core-shell yarns composed of a single conductive yarn and different numbers of wrapping yarns. (g) Schematic diagram of weaving the 3D arc-shaped fabric. (h) Physical image of the 3D arc-shaped fabric. (i) Durability test of F-TENG after 10,000 cycles.

The increased diameter of the core-shell yarn with an increased number of conductive yarns and wrapping yarns indicates that there is no gap between conductive yarns and wrapping yarns (Fig. 3c). That is to say, the conductive yarn is tightly wrapped by the wrapping yarn. Fig. 3d illustrates the voltage output for different numbers of wrapping yarns and conductive yarns. Under the same length, the single conductive yarn and eight wrapping yarns exhibit the highest voltage output, which is consistent with the results in Fig. 3b. Fig. 3e demonstrates the voltage output of core-shell yarns composed of a single conductive yarn

and eight wrapping yarns, at different lengths, showing an increased voltage output with increasing yarn length. This is because the longer the core-shell yarn, the greater the contact area, leading to more charges accumulating on the surface of the wrapping yarn. Consequently, a higher output is achieved as the charges are transferred through the central conductive yarn. Fig. 3f presents the force-displacement curves for single conductive yarn and different numbers of wrapping yarns, indicating that the addition of wrapping yarns enhances the strength of the entire core-shell yarn. Through theoretical calculation and

experimental examination, we ultimately selected core-shell yarns composed of a single conductive yarn and eight wrapping yarns for braiding, resulting in a 3D arc-shaped fabric (Fig. 3g and Fig. 3h). The fabric loading diagram, grain plate diagram, heddle threading diagram, and reed threading diagram are shown in Fig. S3. After the arc fabric is woven, the wool-connected conductive yarns are one electrode and the PI-connected conductive yarns are the other electrode, with the conductive yarns connected in parallel. When pressure brings the surfaces of the two materials into contact, electrons flow through the load between the two electrodes, creating an electric current. Moreover, to verify the durability of the F-TENG device, 10,000 reciprocating motion cycles were performed, with only a 9 % decline in performance observed, indicating its good durability (Fig. 3i).

3.2. Regulation of output performance of 3D F-TENG by projection ratio

Traditional 3D flexible-based TENGs generally operates in the contact-separation mode, where their electrical outputs are correlated with the effective contact area and contact-separation distance [37,38]. To compare different arc structures, we adjusted the projection ratio P to simultaneously modulate the coupling effect of the effective contact area and contact-separation distance.

Fig. 4 (a1-a5) depict the schematic diagrams of the samples with different projection ratios (P ranging from 1.2 to 2.0 with a sample interval of 0.2). Fig. 4 (b1-b5) show corresponding physical images of the samples with increasing P . Under the same bottom width, the height of

the arc structure increases with P (b1-b5). Fig. 4 (c1-c5) demonstrate the compression of the arc structure. When P reaches 1.6 (Fig. 4c3), the increase in height and arc length of the arc structure leads to a decrease in the effective contact area, thereby reducing the generation of surface-induced charges [39].

Fig. 4 (d1-d5) show the COMSOL simulation images of different P samples after compression, validating the shape change of the compressed 3D F-TENG (Fig. S4). Fig. 4 (e1-e5) show the voltage output of the samples with different P . As P increases, the voltage output exhibits a trend of initially increasing and then decreasing, rising from 2.8 V ($P=1.2$) to 4.8 V ($P=1.6$) before decreasing to 2.6 V ($P=2.0$). Notably, the voltage output of the 3D F-TENG at $P=1.6$ is 3 times higher than that of the traditional double-plane model, and the output current is 2.6 times higher than that of the traditional double-plane model (Fig. S5). This simultaneously validates that the TENG's output is not only related to the movement displacement between the triboelectric layers but also to the contact area (Fig. 4c3). The synergistic effect of the two parameters is optimal at $P=1.6$, thereby resulting in the best electrical output (Fig. 4e3).

The sample with $P=1.6$ is connected to a rectifier bridge and a capacitor to supply power to electronic devices. The circuit diagram is depicted in Fig. 5a. Fig. 5b demonstrates that the alternating current generated by the 3D F-TENG, after rectification and energy storage, allows the stopwatch timer to function normally (Video V1). The energy storage curve of the capacitor is illustrated in Fig. 5c, indicating that energy storage via the capacitor can provide the necessary energy

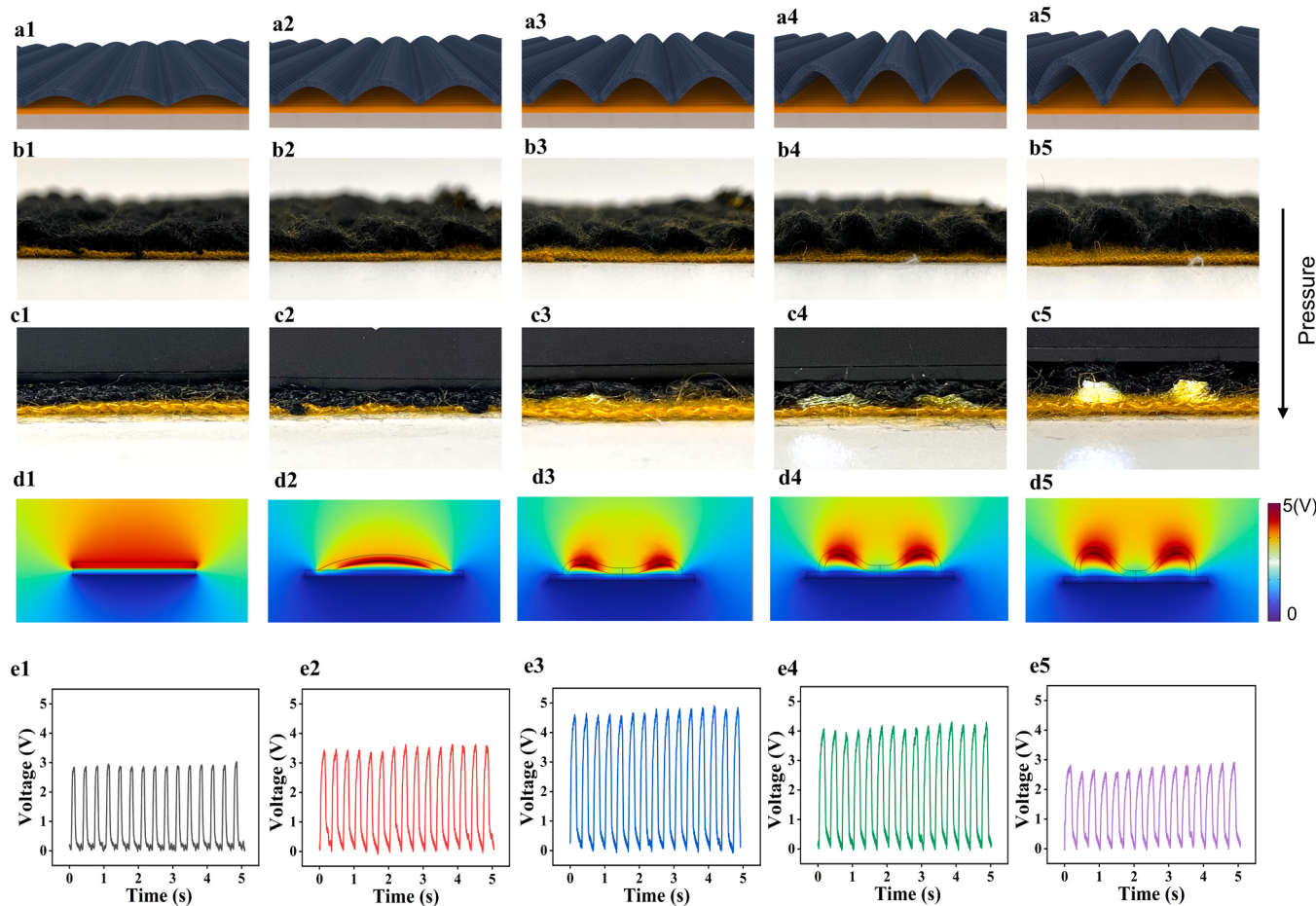


Fig. 4. Illustrates the regulation pattern and mechanism of the electrical output of 3D F-TENG based on the projection ratio. Schematic diagrams of models with different projection ratios, namely $P=1.2$ (a1), $P=1.4$ (a2), $P=1.6$ (a3), $P=1.8$ (a4), and $P=2.0$ (a5), are presented. Corresponding physical images of the samples with different P are depicted in (b1-b5). The compression diagrams of the samples with different P are shown in (c1-c5). After compression, COMSOL simulation images of the samples with different P are displayed in (d1-d5). The voltage output of the samples with different P is presented in (e1-e5).

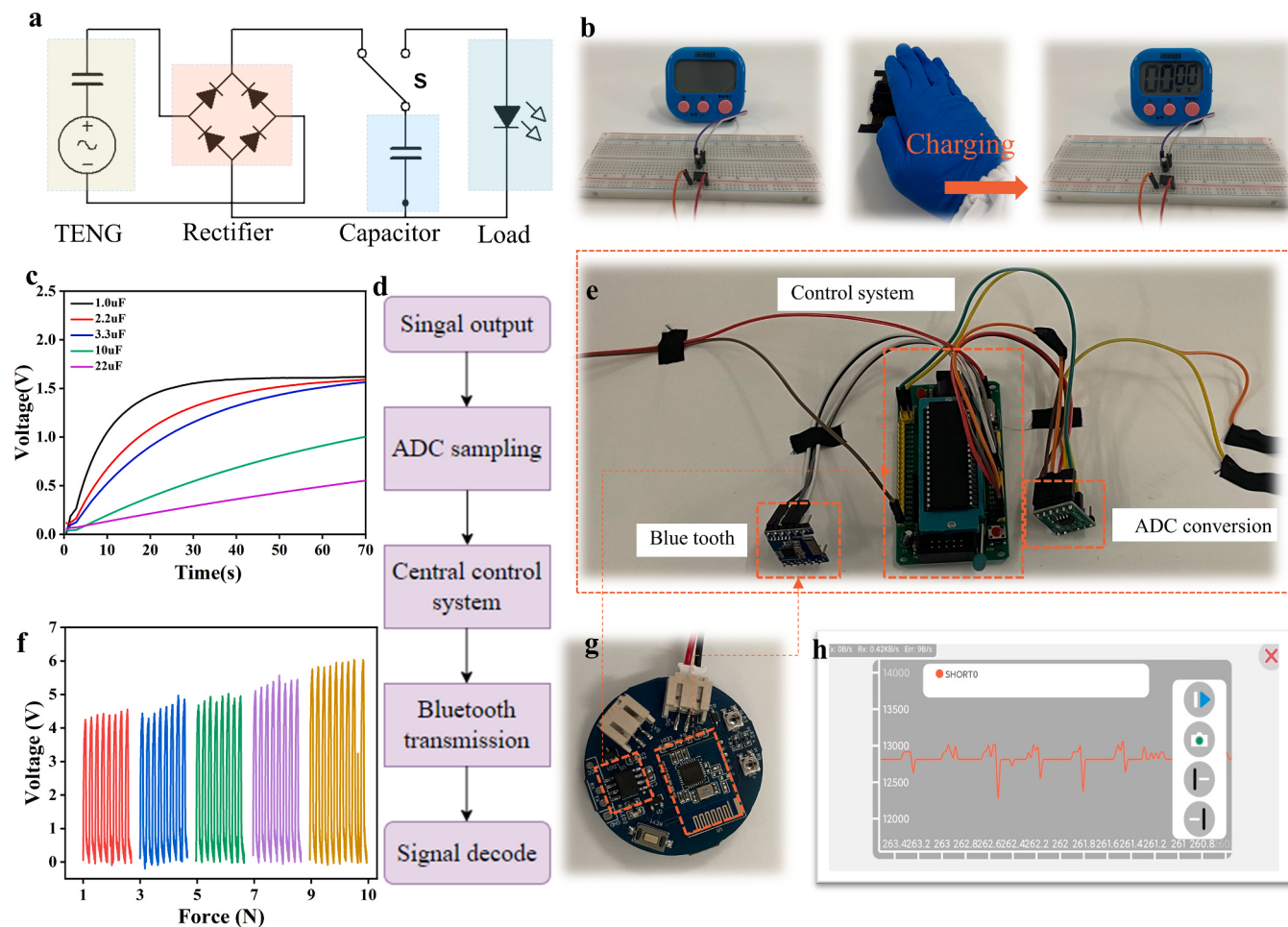


Fig. 5. Illustrates the load driving and wireless sensing applications of the 3D F-TENG. (a) Schematic diagram of the rectification power supply circuit. (b) Driving electronic devices. (c) Charging and discharging curve of the capacitor. (d) Logic diagram of wireless real-time sensing. (e) Physical connection circuit diagram of wireless real-time sensing. (f) Voltage output under different forces. (g) Integrated module of wireless real-time sensing PCB. (h) Mobile app interface displaying wireless real-time sensing.

support for low-power electronic devices.

Supplementary material related to this article can be found online at doi:10.1016/j.nanoen.2024.110000.

Additionally, we utilized microcontrollers and Bluetooth modules to transmit the collected signals to a mobile terminal in real-time, achieving real-time monitoring of the collected signals by mobile phone. The logic diagram of the wireless real-time sensing is shown in Fig. 5d. Fig. 5e displays the physical connection diagram of the wireless real-time sensing system, where the collected signals are converted to digital signals through an ADC and transmitted to the microcontroller control system. The microcontroller then transmits the processed signals to the Bluetooth module via serial communication, and the Bluetooth module wirelessly transmits them to the mobile phone. Fig. 5f demonstrates the variation of voltage with different compression stresses, indicating that the voltage output is proportional to the force applied to the 3D F-TENG. Fig. 5g shows the integrated micro-PCB board of various modules, improving the stability of signal acquisition, conversion, and transmission, as shown in Fig. S6. Fig. 5h displays the real-time signals received by the mobile terminal, demonstrating good performance for biomechanical sensing (Video V2). In summary, the 3D F-TENG exhibits excellent output performance in both supplying power to electronic devices and biomechanical sensing, providing insights into energy supply and sensing technology in wearable devices.

Supplementary material related to this article can be found online at doi:10.1016/j.nanoen.2024.110000.

3.3. The angle dependence of electrical output

After selecting the sample with the optimal electrical output ($P=1.6$), we compared the electrical output of traditional 3D flexible-based TENG with that of 3D F-TENG at different angles. Using a self-designed knob-style platform (Fig. S7), we measured the output performance of the two sets of samples at various angles. Corresponding experimental data are shown in Fig. 6 (a1-a5) reveal the compressed morphology of traditional 3D fabric at 30° , 60° , 90° , 120° , and 150° , while b1-b5 show the corresponding COMSOL simulation results (Fig. S8). Similarly, Fig. 6 (c1-c5) and d1-d5 display the compressed morphology and corresponding COMSOL simulation results (Fig. S9) of 3D F-TENG at different angles. Additionally, we used Abaqus software to simulate the stress on the arc structure at different angles and verified the deformation status of the arc structure after pressing (Fig. S10). To verify the weakened angle-dependence of F-TENG between energy collection efficiency and motion angle in more dimensions, the voltage output and its attenuation in both x-z and y-z planes (Fig S11) are shown in Fig. 6e-f and Figs. S12.

By comparing the data in Figs. 6e and 6f, we found that when the force angle is perpendicular to the surface of the triboelectric layer (90°), the voltage output of both sets of samples reaches its maximum value, namely 1.3 V and 8.1 V, respectively. However, when compressive stresses at non-vertical angles are applied to the triboelectric layer, we observe that the voltage outputs of the two samples are attenuated with varied degrees (Fig. 6e). Taking the mean value of the highest voltage output of the respective samples at $\theta=90^\circ$ as 100 %, the

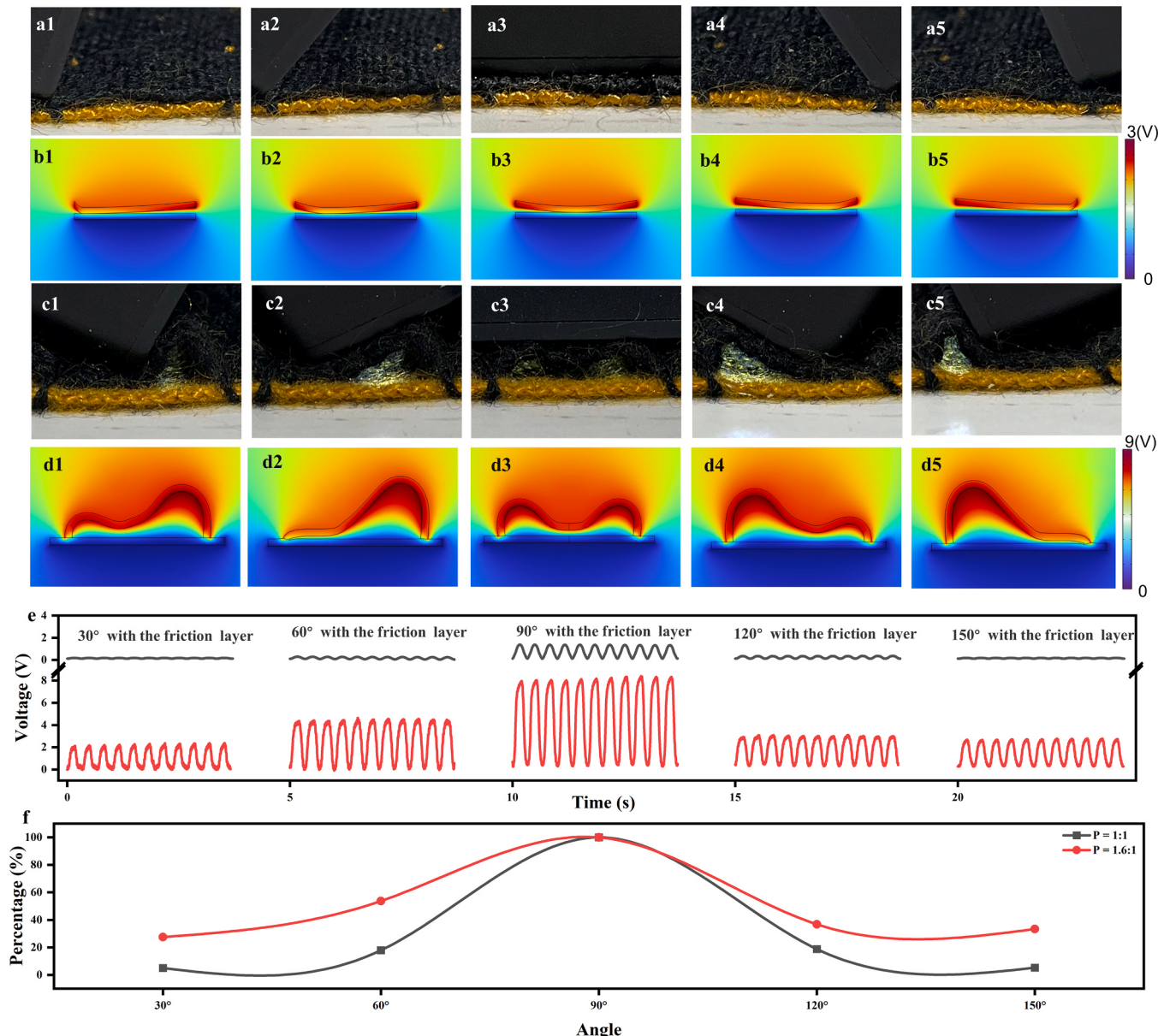


Fig. 6. Illustrates the relationship between the voltage output of traditional 3D flexible-based TENG and 3D F-TENG as a function of angle variation: (a1-a5) depict the digital photos of traditional 3D flexible-based TENG under applied pressure; (b1-b5) illustrate corresponding simulated diagrams of traditional 3D flexible-based TENG under applied pressure; (c1-c5) present the digital photos of 3D F-TENG under applied pressure; (d1-d5) demonstrate simulated diagrams of 3D F-TENG under applied pressure; (e) displays the voltage output of traditional 3D flexible-based TENG and 3D F-TENG at different angles of applied force in a x-z plane; (f) compares the voltage attenuation amplitude of traditional 3D flexible-based TENG and 3D F-TENG under various angles of applied force in a x-z plane.

maximum voltage output of the 3D F-TENG is 35.5 % higher than that of the traditional 3D flexible-based TENG at the same angle ($0 \neq 90^\circ$) (Fig. 6f). Moreover, at different angles of force, the output of the 3D F-TENG exhibits better linearity (Fig. 6f), indicating its superior potential for sensing applications.

Similar data patterns inside a x-z plane with that inside a y-z plane further verify that F-TENG is more efficient than traditional 3D flexible TENG in harvesting energy at multiple angles. Integrating 3D F-TENG into everyday textiles such as gloves, wristbands, and knee pads enables all-direction and efficient harvesting of mechanical energy generated by human activities. Fig. 7 illustrates this integration: Fig. 7(a1-a3) depicts the digital photos of traditional 3D flexible-based TENG at different joint sites of the human body, with voltage output displayed in Fig. 7(b1-b3); while Fig. 7(c1-c3) show the digital photos of 3D F-TENG at equivalent positions, with voltage output shown in Fig. 7(d1-d3). It was further

observed that the flexible TENG had a higher output voltage at a limb bending angle of 90° . As the bending angle increases, more force is required to deform the fabric, which endows the flexible TENG with a high output performance at a bending angle of 120° .

By comparing the voltage output of the two samples integrated at different joint sites, it is found that the 3D F-TENG has a superior electrical output at different compressive stress angles such as finger bending and stretching compared to the traditional 3D flexible-based TENG. This implies that during diverse and irregular movements of the human body, 3D F-TENG can harvest mechanical energy more effectively, providing stable energy sources for self-powered sensing. Additionally, we conducted a fitting analysis of the voltage output from different areas (Fig. S13). It was found that 3D F-TENG exhibits better linearity in voltage output, suggesting potential applications in intelligent monitoring in daily life, thereby offering more convenience and

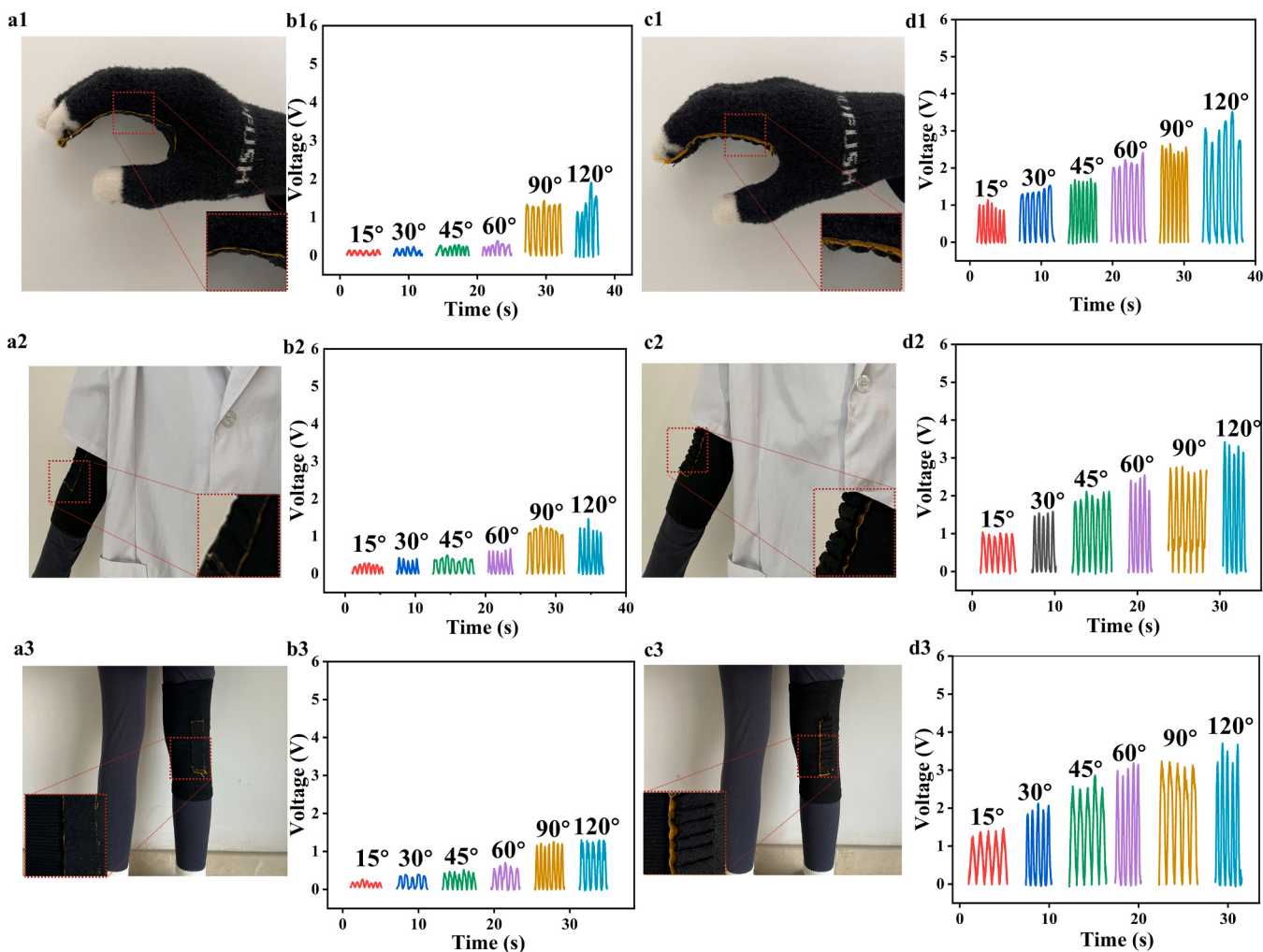


Fig. 7. Illustrates the sensory applications of various joints in the human body. (a1-a3) showcase the digital photos of traditional 3D flexible-based TENG integrated into gloves, elbow pads, and knee pads, along with the corresponding voltage output at the respective joint areas (b1-b3); while (c1-c3) depict the digital photos of 3D F-TENG integrated into gloves, elbow pads, and knee pads, along with the corresponding voltage output at the respective joint areas (d1-d3).

accurate healthcare.

4. A highly accurate plantar pressure sensing system

The integration of self-powered sensing with healthcare holds great promise, potentially advancing internet-based medical services and scientific monitoring of human health to a higher level of digitization and precision [40,41]. 3D F-TENG can be seamlessly incorporated into textiles such as insoles and wristbands, effectively converting biomechanical energy into electrical power [23]. For instance, during physical activities, various postures exert distinct pressures on different areas of the foot. By integrating flexible-based TENGs with insoles, the electrical signals from different regions of the foot can be utilized to identify human movement patterns, thereby gaining insights into body activity. Analyzing these data enables the recording of steps, activity levels, and health status, providing personalized fitness tracking services to users [42,43]. Such personalized services facilitate better health management and aid in preventing the onset of chronic diseases.

In this study, a novel 3D F-TENG insole was used for posture recognition and human motion detection (Fig. 8). Fig. 8a illustrates the distribution of pressure detection points on the insole, with a total of 12 pressure sensing units integrated across the entire insole, each with independent channels. The combination of voltage outputs from these units enables accurate recognition of 5 different postures (Fig. 8b). By

leveraging 1200 sets of collected waveform data and utilizing the YOLOv5 algorithm for learning and training, we obtained the confusion matrix of the model. The recognition accuracy for the 5 different postures reached 86.8 % (Fig. 8c), marking a 37.8 % improvement over the recognition accuracy of traditional 3D flexible-based TENG insoles (Fig. S14). Furthermore, we observed that during posture 2, posture 5, or dynamic running processes, the sensing units 2, 3, 8, and 9 of traditional 3D flexible-based TENG only exhibited noticeable voltage output when the foot was fully flexed. In contrast, the 3D F-TENG maintained continuous and excellent output performance throughout the dynamic process of foot deformation. This indicates that 3D F-TENG exhibits weaker dependence on the harvesting of biological dynamic energy, validating its potential application for the efficient collection of biomechanical energy from various angles and providing a more intelligent and personalized solution for smart health management. Finally, the experimental results also show that the recognition accuracy of the filtered traditional flexible 3D-TENG insoles and F-TENG insoles decreased from 49 % (Fig. S14c) and 86.8 % (Figs. 8c) to 18.2 % (Fig. S15c) and 82.6 % (Fig. S16c), respectively. We believe that the filtering process removed some characteristic signals, leading to a reduction in accuracy. Therefore, for machine learning recognition of TENGs, we recommend using pre-filtered signals to improve recognition accuracy.

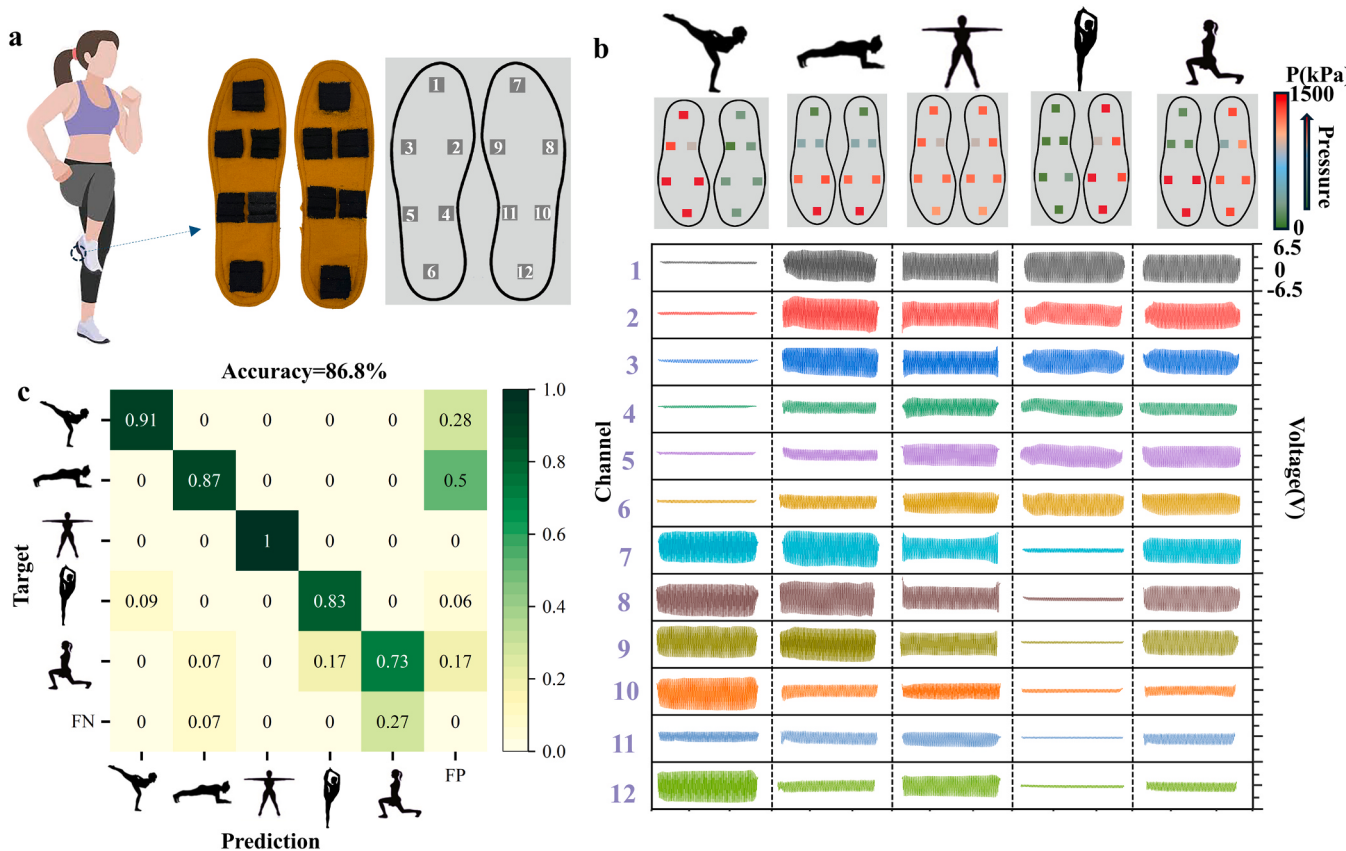


Fig. 8. Plantar pressure sensing with 3D F-TENG. (a) Schematic diagram of the foot pressure sensing system; (b) Plantar pressure mapping distribution and voltage output signals for five typical postures; (c) Confusion matrix of outputs for five typical postures, achieving an overall accuracy rate of 86.8 %.

5. Conclusion

In summary, this study developed a novel 3D F-TENG. This 3D flexible arc-shaped structure breaks through the boundary limitation of traditional 3D flexible structures in the unit shift direction and can still produce effective output when subjected to compressive forces in different directions. It demonstrates the capability to efficiently collect energy from all directions, thus advancing the practical application of flexible-based TENGs. By modulating the projection ratio P , it effectively coordinates the relative motion distance and effective contact area. At $P=1.6$, its voltage output is 3 times higher than that of traditional 3D flexible-based TENG, and the corresponding output current is 2.6 times higher. Compared to traditional contact-separation-based 3D flexible-based TENG, the 3D F-TENG enhances energy collection efficiency by 35.5 % for non-vertical movements, enabling efficient biomechanical energy harvesting and self-powered sensing from human irregular and complex movements. Additionally, we integrated traditional 3D flexible-based TENG and 3D F-TENG into textile structures such as gloves, protective gear, and insoles. We found that under different bending angles, the 3D F-TENG exhibited superior linear output and higher recognition accuracy (37.8 % higher than traditional 3D flexible-based TENG). The 3D F-TENG offers a simple fabrication process suitable for large-scale mechanized production, showcasing the enormous potential for efficient collection of mechanical energy from various human movements.

6. Design and methodology

6.1. Materials

The PI yarn (40 S/2) is produced by Taihe New Materials Co., Ltd.,

the 72 N/2 wool fiber yarn (72 N/2) is manufactured by Shandong Ruyi Co., Ltd., and the anti-static silver-plated conductive nylon yarn (140D) is fabricated by Jiangxi Copper Corporation Limited.

6.2. Fabrication of core-shell yarn

Using the high-speed braiding machine (KBL-90-16-1, China) manufactured by Xuzhou Henghui Braiding Machinery Co., Ltd. as the experimental equipment, we investigated the relationship between the electrical output of silver nanowire conductive yarn and PI/wool wrapping yarn. On a high-speed braiding machine, core-shell structured fibers are formed through rotational braiding (Fig. 3a). The conductive material chosen is commercial silver-plated nylon, while the dielectric materials are wool and PI. Firstly, the conductive nylon yarn is secured on the central axis, followed by wrapping the PI/wool yarn around the spool. Finally, it is anchored on the machine bed. During the operation of the high-speed braiding machine, the spools rotate clockwise and counterclockwise. Different spools, due to their opposite rotation directions, intertwine and wrap around each other, forming the core-shell structured fibers. Continuous collection of the core-shell yarn is facilitated by the winding device at the top of the braiding machine. The continuous supply of yarn is through the lifting and rotation of the spindles, and the quantity of wound yarn depends on the number of spindles on the machine bed.

6.3. The preparation of 3D F-TENG

To ensure the accuracy of the experimental process, we utilized the high-speed sectional warping machine (KGA269C) produced by Jinyang Sixing Machinery Co., Ltd. to warp the core-shell yarn, and the core-shell yarn was woven using the rapier loom (SGA598) from

Jiangyin Tongyuan Textile Co., Ltd. To maintain the consistency of the warp and weft density during the weaving of 3D arc fabrics, a dual warp beam feeding system is employed, and the warp and weft yarns on the rapier loom are systematically interlaced in different directions. The threading, rapiers, pattern plates, and weaving diagrams of the 3D arc fabric are shown in S3. During the process of weaving the weft, the curling device in front of the rapier loom curls the warp yarns regularly. According to the weaving diagram, every 30-weft insertion constitutes one cycle. The specifications of the protrusions between different samples are adjusted by regulating the weft density and the number of weft insertions. The tightness of the fabric depends on the settings of the warp and weft densities.

6.4. Characterization and measurement

We employed a linear drive motor (LPS1, China) to apply repeated force to both traditional 3D flexible-based TENG and 3D F-TENG to ensure the repeatability of the experimental measurements. We provided detailed design and model diagrams of the linear motor mechanical arm rotary rod for multi-angle measurements using LPS1 in Figs. S7 and S11. Furthermore, in an ambient temperature environment with a frequency of 3 Hz and a contact force of 5 N, we measured the electrical output of different fabric TENG using a Keithley 6514 electrostatic meter (Agitek, China). We observed the cross-sectional morphology of the core-shell yarn using a scanning electron microscope (SU-8010) produced by the Japanese company, Hitachi High-Tech Corporation, and observed the surface morphology using a 3D digital microscope (R-405-OL) from HiROX Co., Ltd. Additionally, we measured the diameter of the core-shell yarn using a digital caliper (Syntek) produced by Deqing Shengtai Xin Electronic Technology Co., Ltd., and observed the stress-strain curves of different core-shell yarns using a universal material testing machine (INSTRON594) from the American company, Instron. Finally, we conducted modeling and simulation using COMSOL Multiphysics software.

CRediT authorship contribution statement

Dali Yan: Writing – original draft, Investigation, Formal analysis, Data curation. **Dan Tao:** Methodology, Formal analysis. **Jian Fang:** Writing – review & editing. **Weilin Xu:** Writing – review & editing. **Duo Xu:** Methodology, Investigation, Data curation. **Yirong Sun:** Formal analysis. **Bo Deng:** Writing – review & editing, Supervision, Conceptualization. **Genyang Cao:** Supervision.

Declaration of Competing Interest

The authors declare that they have no known competing financial interests or personal relationships that could have appeared to influence the work reported in this paper.

Data availability

Data will be made available on request.

Acknowledgments

This work was supported by the National Natural Science Foundation of China (U21A2095, 52173059); the Key Research and Development Program of Hubei Province (2021BAA068); the Major Basic Research Project of the Natural Science Foundation of the Jiangsu Higher Education Institutions (21KJA540002).

Appendix A. Supporting information

Supplementary data associated with this article can be found in the online version at [doi:10.1016/j.nanoen.2024.110000](https://doi.org/10.1016/j.nanoen.2024.110000).

References

- [1] C. Zhi, S. Shi, S. Meng, H. Wu, Y. Si, K. Zhang, S. Zhang, J. Hu, A biocompatible and antibacterial all-textile structured triboelectric nanogenerator for self-powered tactile sensing, *Nano Energy* 115 (2023) 108734, <https://doi.org/10.1016/j.nanoen.2023.108734>.
- [2] Y. Pang, X. Zhu, Y. Jin, Z. Yang, S. Liu, L. Shen, X. Li, C. Lee, Textile-inspired triboelectric nanogenerator as intelligent pavement energy harvester and self-powered skid resistance sensor, *Appl. Energy* 348 (2023) 121515, <https://doi.org/10.1016/j.apenergy.2023.121515>.
- [3] Z. Sun, Y. Hu, W. Wei, Y. Li, Q. Zhang, K. Li, H. Wang, C. Hou, Hyperstable eutectic core-spun fiber enabled wearable energy harvesting and personal thermal management fabric, *Adv. Mater.* 36 (2024) 2310102, <https://doi.org/10.1002/adma.202310102>.
- [4] X. Gong, M. Ding, P. Gao, X. Liu, J. Yu, S. Zhang, B. Ding, High-performance liquid-repellent and thermal-wet comfortable membranes using triboelectric nanostructured nanofiber/meshes, *Adv. Mater.* 35 (2023) 2305606, <https://doi.org/10.1002/adma.202305606>.
- [5] J. Zhong, Y. Zhang, Q. Zhong, Q. Hu, B. Hu, Z.L. Wang, J. Zhou, Fiber-based generator for wearable electronics and mobile medication, 6273-80, *ACS Nano* 8 (2014), <https://doi.org/10.1021/nn501732z>.
- [6] J. Yi, K. Dong, S. Shen, Y. Jiang, X. Peng, C. Ye, Z.L. Wang, Fully fabric-based triboelectric nanogenerators as self-powered human-machine interactive keyboards, *Nano Micro Lett.* 13 (2021) 103, <https://doi.org/10.1007/s40820-021-00621-7>.
- [7] M.Y. So, B. Xu, Z. Li, C.L. Lai, C. Jiang, Flexible corrugated triboelectric nanogenerators for efficient biomechanical energy harvesting and human motion monitoring, *Nano Energy* 106 (2023) 108033, <https://doi.org/10.1016/j.nanoen.2022.108033>.
- [8] C. Gui, R. Zhang, Z. Chen, W. Wu, H. Li, J. Huang, Textile-based triboelectric nanogenerators via electroless plating for fabricating electrode material: study of the relationship between electrostatic-charge density and strain in dielectric material, *Compos. Sci. Technol.* 218 (2022) 109187, <https://doi.org/10.1016/j.compscitech.2021.109187>.
- [9] M. Li, B. Xu, Z. Li, Y. Gao, Y. Yang, X. Huang, Toward 3D double-electrode textile triboelectric nanogenerators for wearable biomechanical energy harvesting and sensing, *Chem. Eng. J.* 450 (2022) 137491, <https://doi.org/10.1016/j.cej.2022.137491>.
- [10] K.Y. Lee, H.-J. Yoon, T. Jiang, X. Wen, W. Seung, S.-W. Kim, Z.L. Wang, Fully packaged self-powered triboelectric pressure sensor using hemispheres-array, *Adv. Energy Mater.* 6 (2016) 1502566, <https://doi.org/10.1002/aenm.201502566>.
- [11] X. Peng, K. Dong, C. Ye, Y. Jiang, S. Zhai, R. Cheng, D. Liu, X. Gao, J. Wang, Z.L. Wang, A breathable, biodegradable, antibacterial, and self-powered electronic skin based on all-nanofiber triboelectric nanogenerators, *Sci. Adv.* 6 eaba9624, <https://doi.org/10.1126/sciadv.eaba9624>.
- [12] H. Guo, Q. Fei, M. Lian, T. Zhu, W. Fan, Y. Li, L. Sun, F. de Jong, K. Chu, W. Zong, C. Zhang, T. Liu, Weaving aerogels into 3D ordered hyperelastic hybrid carbon assemblies, *Adv. Mater.* 35 (2023) 2301418, <https://doi.org/10.1002/adma.202301418>.
- [13] X. Shi, S. Zhang, S. Gong, A self-powered and arch-structured triboelectric nanogenerator for portable electronics and human-machine communication, *J. Mater. Chem. A* 8 (2020) 8997–9005, <https://doi.org/10.1039/DOTA02178D>.
- [14] D. Yan, J. Ye, Y. Zhou, X. Lei, B. Deng, W. Xu, Research progress of fabrics with different geometric structures for triboelectric nanogenerators in flexible and wearable electronics, 1852-78, *Adv. Fiber Mater.* 5 (2023), <https://doi.org/10.1007/s42765-023-00334-z>.
- [15] Z. Ding, W. Li, W. Wang, Z. Zhao, Y. Zhu, B. Hou, L. Zhu, M. Chen, L. Che, Highly sensitive iontronic pressure sensor with side-by-side package based on alveoli and arch structure, *Adv. Sci. N./a* (2024) 2309407, <https://doi.org/10.1002/advs.202309407>.
- [16] Z. Qu, M. Huang, C. Chen, Y. An, H. Liu, Q. Zhang, X. Wang, Y. Liu, W. Yin, X. Li, Spherical triboelectric nanogenerator based on eccentric structure for omnidirectional low frequency wave energy harvesting, *Adv. Funct. Mater.* 32 (2022) 2202048, <https://doi.org/10.1002/adfm.2022202048>.
- [17] X. Liang, T. Jiang, G. Liu, T. Xiao, L. Xu, W. Li, F. Xi, C. Zhang, Z.L. Wang, Triboelectric nanogenerator networks integrated with power management module for water wave energy harvesting, *Adv. Funct. Mater.* 29 (2019) 1807241, <https://doi.org/10.1002/adfm.201807241>.
- [18] W. Paosangthong, M. Wagih, R. Torah, S. Beeby, Textile-based triboelectric nanogenerator with alternating positive and negative freestanding woven structure for harvesting sliding energy in all directions, *Nano Energy* 92 (2022) 106739, <https://doi.org/10.1016/j.nanoen.2021.106739>.
- [19] B. Zhu, H. Wu, H. Wang, Z. Quan, H. Luo, L. Yang, R. Liao, J. Wang, Spherical 3D fractal structured dual-mode triboelectric nanogenerator for multidirectional low-frequency wave energy harvesting, *Nano Energy* 124 (2024) 109446, <https://doi.org/10.1016/j.nanoen.2024.109446>.
- [20] L. Shang, Z. Wu, X. Li, A. Xu, Y. Miao, W. Xu, W. Tang, C. Fu, B. Su, K. Dong, Z. Xia, A breathable and highly impact-resistant shear-thickened fluid (STF) based TENG via hierarchical liquid-flow spinning for intelligent protection, *Nano Energy* 118 (2023) 108955, <https://doi.org/10.1016/j.nanoen.2023.108955>.
- [21] D. Tan, B. Xu, Y. Gao, Y. Tang, Y. Liu, Y. Yang, Z. Li, Breathable fabric-based triboelectric nanogenerators with open-porous architected polydimethylsiloxane coating for wearable applications, *Nano Energy* 104 (2022) 107873, <https://doi.org/10.1016/j.nanoen.2022.107873>.
- [22] X. Peng, K. Dong, Y. Zhang, L. Wang, C. Wei, T. Lv, Z.L. Wang, Z. Wu, Sweat-permeable, biodegradable, transparent and self-powered chitosan-based electronic

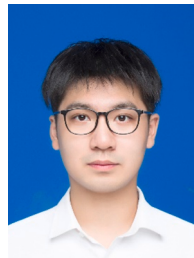
- skin with ultrathin elastic gold nanofibers, *Adv. Funct. Mater.* 32 (2022) 2112241, <https://doi.org/10.1002/adfm.202112241>.
- [23] G. Xu, X. Huang, R. Shi, Y. Yang, P. Wu, J. Zhou, X. He, J. Li, Y. Zen, Y. Jiao, B. Zhang, J. Li, G. Zhao, Y. Liu, Y. Huang, M. Wu, Q. Zhang, Z. Yang, X. Yu, Triboelectric nanogenerator enabled sweat extraction and power activation for sweat monitoring, *Adv. Funct. Mater.* 34 (2024) 2310777, <https://doi.org/10.1002/adfm.202310777>.
- [24] G. Yang, H. Li, R. Xing, M. Lv, C. Ma, J. Yan, X. Zhuang, Thermal-triggered “on-off” switchable triboelectric nanogenerator based on two-way shape memory polymer, *Adv. Funct. Mater.* 33 (2023) 2214001, <https://doi.org/10.1002/adfm.202214001>.
- [25] K. Xia, J. Fu, Z. Xu, Multiple-frequency high-output triboelectric nanogenerator based on a water balloon for all-weather water wave energy harvesting, *Adv. Energy Mater.* 10 (2020) 2000426, <https://doi.org/10.1002/aenm.202000426>.
- [26] C. Ye, Q. Xu, J. Ren, S. Ling, Violin string inspired core-sheath silk/steel yarns for wearable triboelectric nanogenerator applications, *Adv. Fiber Mater.* 2 (2020) 24–33, <https://doi.org/10.1007/s42765-019-00023-w>.
- [27] G. Liu, S. Xu, Y. Liu, Y. Gao, T. Tong, Y. Qi, C. Zhang, Flexible drug release device powered by triboelectric nanogenerator, *Adv. Funct. Mater.* 30 (2020) 1909886, <https://doi.org/10.1002/adfm.201909886>.
- [28] T. Jing, B. Xu, J.H. Xin, X. Guan, Y. Yang, Series to parallel structure of electrode fiber: an effective method to remarkably reduce inner resistance of triboelectric nanogenerator textiles, 12331-9, *J. Mater. Chem. A* 9 (2021), <https://doi.org/10.1039/DITA01309B>.
- [29] L. Dong, M. Wang, J. Wu, C. Zhu, J. Shi, H. Morikawa, Deformable textile-structured triboelectric nanogenerator knitted with multifunctional sensing fibers for biomechanical energy harvesting, *Adv. Fiber Mater.* 4 (2022) 1486–1499, <https://doi.org/10.1007/s42765-022-00181-4>.
- [30] L. Feng, S. Xu, T. Sun, C. Zhang, J. Feng, L. Yao, J. Ge, Fire/acid/alkali-resistant aramid/carbon nanofiber triboelectric nanogenerator for self-powered biomotion and risk perception in fire and chemical environments, *Adv. Fiber Mater.* 5 (2023) 1478–1492, <https://doi.org/10.1007/s42765-023-00288-2>.
- [31] F. Xing, Z. Ou, X. Gao, B. Chen, Z.L. Wang, Harvesting electrical energy from high temperature environment by aerogel nano-covered triboelectric yarns, *Adv. Funct. Mater.* 32 (2022) 2205275, <https://doi.org/10.1002/adfm.202205275>.
- [32] K.G. Motorca, C.-M. Wu, C.R.M. Jose, G.M. Rani, Waste-to-energy: development of a highly efficient keratin enhanced chitosan bio-waste-derived triboelectric nanogenerator for energy harvesting and real applications, *Adv. Funct. Mater.* n/a (2024) 2315069, <https://doi.org/10.1002/adfm.202315069>.
- [33] Q. Zhang, K. Barri, S.R. Kari, Z.L. Wang, A.H. Alavi, Multifunctional triboelectric nanogenerator-enabled structural elements for next generation civil infrastructure monitoring systems, *Adv. Funct. Mater.* 31 (2021) 2105825, <https://doi.org/10.1002/adfm.202105825>.
- [34] K. Shi, B. Chai, H. Zou, Z. Wen, Y. Liu, M. He, J. Chen, P. Jiang, X. Huang, Direct-current triboelectric nanogenerators based on contact-separation mode and conductive-adhesive interface, *Adv. Funct. Mater.* n/a (2024) 2400204, <https://doi.org/10.1002/adfm.202400204>.
- [35] M. Sala de Medeiros, D. Chanci, C. Moreno, D. Goswami, R.V. Martinez, Waterproof, breathable, and antibacterial self-powered e-textiles based on omniphobic triboelectric nanogenerators, *Adv. Funct. Mater.* 29 (2019) 1904350, <https://doi.org/10.1002/adfm.201904350>.
- [36] K. Dong, X. Peng, J. An, A.C. Wang, J. Luo, B. Sun, J. Wang, Z.L. Wang, Shape adaptable and highly resilient 3D braided triboelectric nanogenerators as e-textiles for power and sensing, *Nat. Commun.* 11 (2020) 2868, <https://doi.org/10.1038/s41467-020-16642-6>.
- [37] Z. Zheng, D. Yu, Y. Guo, Dielectric modulated glass fiber fabric-based single electrode triboelectric nanogenerator for efficient biomechanical energy harvesting, *Adv. Funct. Mater.* 31 (2021) 2102431, <https://doi.org/10.1002/adfm.202102431>.
- [38] Q. Mu, W. He, C. Shan, S. Fu, S. Du, J. Wang, Z. Wang, K. Li, C. Hu, Achieving high-efficiency wind energy harvesting triboelectric nanogenerator by coupling soft contact, charge space accumulation, and charge dissipation design, *Adv. Funct. Mater.* 34 (2024) 2309421, <https://doi.org/10.1002/adfm.202309421>.
- [39] M. Cui, H. Guo, W. Zhai, C. Liu, C. Shen, K. Dai, Template-assisted electrospun ordered hierarchical microhump arrays-based multifunctional triboelectric nanogenerator for tactile sensing and animal voice-emotion identification, *Adv. Funct. Mater.* 33 (2023) 2301589, <https://doi.org/10.1002/adfm.202301589>.
- [40] C. Wei, R. Cheng, C. Ning, X. Wei, X. Peng, T. Lv, F. Sheng, K. Dong, Z.L. Wang, A self-powered body motion sensing network integrated with multiple triboelectric fabrics for biometric gait recognition and auxiliary rehabilitation training, *Adv. Funct. Mater.* 33 (2023) 2303562, <https://doi.org/10.1002/adfm.202303562>.
- [41] H. He, J. Liu, Y. Wang, Y. Zhao, Y. Qin, Z. Zhu, Z. Yu, J. Wang, An ultralight self-powered fire alarm e-textile based on conductive aerogel fiber with repeatable temperature monitoring performance used in firefighting clothing, *ACS Nano* 16 (2022) 2953–2967, <https://doi.org/10.1021/acsnano.1c10144>.
- [42] F. Sun, Y. Zhu, C. Jia, Y. Wen, Y. Zhang, L. Chu, T. Zhao, B. Liu, Y. Mao, Deep-learning-assisted neck motion monitoring system self-powered through biodegradable triboelectric sensors, *Adv. Funct. Mater.* n/a (2023) 2310742, <https://doi.org/10.1002/adfm.202310742>.
- [43] H. Lee, H.E. Lee, H.S. Wang, S.-M. Kang, D. Lee, Y.H. Kim, J.H. Shin, Y.-W. Lim, K. J. Lee, B.-S. Bae, Hierarchically surface-textured ultrastable hybrid film for large-scale triboelectric nanogenerators, *Adv. Funct. Mater.* 30 (2020) 2005610, <https://doi.org/10.1002/adfm.202005610>.



Dali Yan is a graduate student in Materials Science and Engineering at Wuhan Textile University. He received his B.S. degree from the Dezhou University in 2021. His current scientific interests are focused on wearable devices such as triboelectric nanogenerators based on different woven structures.



Dan Tao received her Ph.D. degree in Textile Engineering from School of Textile Science and Engineering, Jiangnan University in 2013. She is currently an assistant professor at Wuhan Textile University. She mainly focuses on functional fibers & textiles.



Duo Xu is currently pursuing his Ph.D. degree at Soochow University. He obtained his B.S. degree from Wuhan Textile University in 2018. His research interests focus on the fabrication of novel multifunctional yarns for applications in smart textiles.



Yirong Sun is a postgraduate at Wuhan Textile University. He graduated with a bachelor's degree from Northeast Petroleum University. His current research interests focus on the impact of textile structures on the performance of triboelectric nanogenerators.



Bo Deng is a professor at the School of Materials Science and Engineering, Wuhan Textile University. He received his PhD degree from Shanghai Institute of Applied Physics, Chinese Academy of Sciences (CAS) in 2008. From 2008–2011, he worked as an associate researcher in the same institute. From 2011–2012, he was a guest scientist with the Paul Scherrer Institute, Switzerland. From 2012–2015, he worked as a post-doctoral researcher at the University of British Columbia, Canada. He is mainly engaged in the research of inorganic nanomaterials for wearable electronics, smart textiles.



Genyang Cao is a professor at the School of Textile Science and Engineering, Wuhan Textile University. He received his Ph. D. degree in textile materials from Donghua University, Shanghai, China, in 2016. His research interests focus on the dyeing technique for high-performance filaments, surface modification and functional finishing on textile fabrics.



Weilin Xu received the Ph.D. degree in textile material from Donghua university, Shanghai, China, in 1997. From 1997–1999, he joined the State Key Laboratory of Polymer Materials Engineering, Sichuan University, Sichuan, China, as a post- doctoral. From 1999–2000, he was a visiting researcher with the Hong Kong Polytechnic University, China. His research interests are intelligent spinning, advanced processing technology, etc. He is currently the Director of the State Key Laboratory of New Textile Materials and Advanced Processing Technologies since 2021. He was elected as a Member of the Chinese Academy of Engineering, in 2021.



Jian Fang received his Ph.D. in Materials Engineering from Deakin University in 2009. He is currently a professor at the College of Textile and Clothing Engineering at Soochow University in China. His research focuses on electro-active fibrous materials for wearable electronics, smart textiles, and energy devices.